J. Fluid Mech. (2010), *vol.* 649, *pp.* 371–398.
doi:10.1017/S0022112009993508

An experimental study of laminar displacement flows in narrow vertical eccentric annuli

S. MALEKMOHAMMADI[1], M. CARRASCO-TEJA[2], S. STOREY[1], I. A. FRIGAARD[1,2]† AND D. M. MARTINEZ[3]

[1]Department of Mechanical Engineering, University of British Columbia, 6250 Applied Science Lane, Vancouver, BC, Canada V6T 1Z4

[2]Department of Mathematics, University of British Columbia, 1984 Mathematics Road, Vancouver, BC, Canada V6T 1Z2

[3]Department of Chemical and Biological Engineering, University of British Columbia, 2360 East Mall, Vancouver, BC, Canada V6T 1Z3

(Received 25 June 2009; revised 14 November 2009; accepted 16 November 2009)

We present an experimental study of slow laminar miscible displacement flows in vertical narrow eccentric annuli. We demonstrate that for suitable choices of viscosity ratio, density ratio and flow rate, we are able to find steady travelling wave displacements along the length of the annulus, even when strongly eccentric. Small eccentricity, increased viscosity ratio, increased density ratio and slower flow rates all appear to favour a steady displacement for Newtonian fluids. Qualitatively similar effects are found for non-Newtonian fluids, although the role of flow rate is less clear. These results are largely in line with predictions of a Hele-Shaw style of displacement model (Bittleston *et al.*, *J. Engng Math.*, vol. 43, 2002, pp. 229–253). The experiments also reveal interesting phenomena caused largely by secondary flows and dispersion. In the steady displacements, eccentricity drives a strong azimuthal counter-current flow above/below the advancing interface. This advects displacing fluid to the wide side of the annulus, where it focuses in the form of an advancing spike. On the narrow side we have also observed a spike, but only in Newtonian fluid displacements. For unsteady displacements, the azimuthal currents diminish as the interface elongates. With a strong enough yield stress and with a large enough eccentricity, unyielded fluid remains behind on the narrow side of the annulus.

1. Introduction

We present an experimental study of slow laminar miscible displacement flows in vertical narrow eccentric annuli. The underlying motivation for the study comes from the oilfield process of primary cementing, which we explain briefly below. The objectives of our study are partly to provide a controlled set of experiments, suitable for exploring the validity of mathematical models of the displacement flow, and partly to consider displacements in parameter ranges having some overlap with field conditions.

Primary cementing is described at length in the recent text by Nelson & Guillot (2006). In this process a steel casing is cemented into a wellbore to ensure a tight hydraulic seal with the outer rock formation. The annular space to be filled with

† Email address for correspondence: frigaard@math.ubc.ca

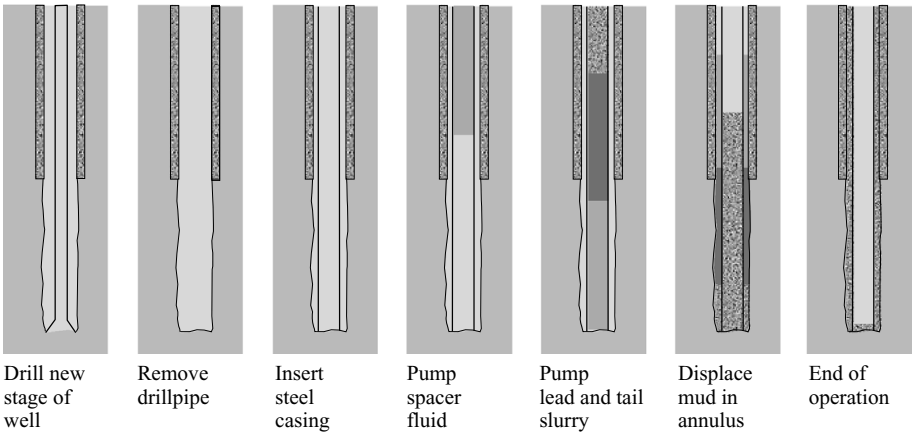

FIGURE 1. Schematic of the primary cementing process, showing the various stages (left to right) in cementing a new casing.

cement is initially full of drilling fluid (or other fluids), which must be removed during the cement placement. The primary cementing process proceeds as follows (see figure 1). A new section of the well is drilled. The drillpipe is removed from the wellbore, leaving drilling mud inside the wellbore. A steel tube (casing or liner) is inserted into the wellbore, typically leaving a gap of ≈ 2 cm between the outside of the tube and the inside of the wellbore, i.e. the annulus. At certain points, *centralizers* are fitted to the outside of the tube to prevent the heavy steel tubing from slumping or sagging to the lower side of the wellbore. However, it is still very common that the annulus is eccentric, especially in inclined wellbores. Once the tube is in place, with drilling mud on the inside and outside, a sequence of fluids are circulated down the inside of the tubing reaching the bottom of the hole and returning up the outside of the annulus. Typically, a wash or spacer fluid is pumped first, followed by one or more cement slurries. The rheologies and densities of the spacer and cement slurries can be designed so as to aid in displacement of the annulus drilling mud. The fluid volumes are designed so that the cement slurries fill the annular space to be cemented. Drilling mud follows the final cement slurry to be pumped and the circulation is stopped with a few metres of cement at the bottom of the inside of the casing (see final figure in figure 1), and the cement is allowed to set. The final part of cement inside the tubing is drilled out as the well proceeds.

From the fluid mechanics perspective, since the volumes of fluids pumped are relatively large, so that successive interfaces are separated, it is reasonable to consider alone the displacement flow between one pair of fluids. Equally, the geometry changes slowly in the axial direction, relative to the scale of the annular gap or circumference, so that consideration of a uniform annulus is also reasonable. Thus, we consider displacement as a flow through a uniform eccentric annulus.

The fluids used in cementing and those that we study are both Newtonian and non-Newtonian. In the latter case we focus mainly on fluids where the behaviour is dominated by a nonlinear shear viscosity, i.e. shear-thinning and yield stress effects. Rudimentary hydraulics-style studies of annular flows for this type of fluid may be found in the technical literature of various industries, dating back to the 1960s or earlier. However, detailed experimental studies of this type of fluid flow in annular geometries are more recent. Probably the best known of these studies

are those by Nouar and Lebouché (e.g. Nouar, Devienne & Lebouché 1987; Naimi, Devienne & Lebouché 1990; Nouar, Desaubry & Zenaidi 1998), those by Nouri and Whitelaw (e.g. Nouri, Umur & Whitelaw 1993; Nouri & Whitelaw 1994, 1997) and the extensive studies of Escudier and coworkers (e.g. Escudier & Gouldson 1995; Escudier, Gouldson & Jones 1995; Escudier *et al.* 2000; Escudier, Oliveira & Pinho 2002*a*). These studies consider fluids similar to those we use here: carboxymethylcellulose (CMC), Xanthan Gum, Carbopol, etc., and cover a wide range of eccentricities, aspect ratios, inner-body rotation rates and Reynolds numbers. Detailed measurements of velocity profiles have been made and in many cases have been compared favourably with computational results. There are also numerous computational studies for these flows and some analytical solutions. The reader is referred to Escudier *et al.* (2002*b*) (which also contains an excellent and comprehensive bibliography) for an overview of this area. Thus, the experimental study of a *single* generalized non-Newtonian fluids, flowing in laminar regime through an annulus, is a mature area.

In terms of eccentric annular *displacement* flows, the experimental literature is much smaller. The first detailed study that we know of was carried out by Tehrani and coworkers: Long (1991); Tehrani, Ferguson & Bittleston (1992); Tehrani, Bittleston & Long (1993). These experiments were carried out in a narrow annulus (aspect ratio: $\delta = 0.035$) of 3 m in length, fully inclinable. Various flow rate and eccentricity combinations were tested, using Xanthan as the representative non-Newtonian fluid. The main measurement method consisted of adding a conductive tracer to one fluid and measuring the fluid conductivity at eight azimuthal positions around the annulus, close to the exit. The conductivity data was used to give the displacing fluid concentration at the exit. This data was compared with model-based output, i.e. in the form of a final displacement efficiency at the end of the experiment. The use of conductivity has some advantages over visualization, in terms of objectivity and the ability to use opaque fluids. On the other hand, the use of a single displacement efficiency to characterize the flow has drawbacks in terms of generalizations to longer annuli. Reasonable qualitative agreement was however found between model predictions and experimental results (see Tehrani *et al.* 1992). A number of interesting flow phenomena were also reported in these studies. Other than the studies by Tehrani and coworkers, there have been only occasional experimental results reported (e.g. Jakobsen *et al.* 1991; Vefring *et al.* 1997; Dutra *et al.* 2004; Nguyen *et al.* 2008).

Our initial interest in annular displacement flows came from revisiting the studies of Tehrani and coworkers. A simple dimensionless analysis of this type of flow, between two non-Newtonian fluids, revealed that as well as Reynolds number, buoyancy number, Péclet number, density ratio, viscosity ratio, eccentricity, aspect ratio and annular inclination, up to four additional dimensionless rheological parameters need considering, i.e. between eight and 12 dimensionless parameters. Without some reduction in parameter space, it was clear that it would be infeasible to study such flows effectively, either experimentally or computationally. The focus chosen was to look at the narrow gap (Hele-Shaw) limit in which inertial effects are negligible and at the high-Péclet-number limit, that is, a limit which is commonly found in the industrial setting. With this the parametric dependence is reduced to five to nine parameters, which is still large for an experimental study. In place of the classical 'displacement efficiency' approach it was decided to first try to understand the dynamics of the displacement flows in this simpler regime, via mathematical modelling, and then use more limited experimental studies to validate the dynamical understanding and illuminate any major shortcomings.

The modelling approach that we have used for these flows is outlined in Bittleston, Ferguson & Frigaard (2002), although the underlying idea of using a Hele-Shaw/porous media approach dates back to Martin, Latil & Vetter (1978) and Tehrani *et al.* (1992). This model has been analysed in depth in the sequence of papers Pelipenko & Frigaard (2004*a*,*b*,*c*), which focus principally at near vertical wells. The dynamics are dominated by the existence (or not) of steady travelling wave solutions, i.e. for certain parameter values the displacement front advects along the annulus at the mean pumping speed. When this does not occur, the front tends to advance faster on the wider side of the annulus and elongates into a finger. Where yield stress fluids are concerned, as is the typical case industrially, it is possible for the fluids to plug the narrow part of the annulus, bridging between inner and outer walls. For limited parameter ranges (near concentric annuli) it is possible to construct analytic solutions to the displacement problem, exhibiting the steady travelling wave behaviour (see Pelipenko & Frigaard 2004*a*). These steady states are in fact found computationally for a much wider range of parameters than those for which it is possible to find analytical solutions (Pelipenko & Frigaard 2004*b*), and it is possible to approximately predict steady and unsteady displacements using a lubrication-style displacement model (see Pelipenko & Frigaard 2004*c*).

In all the above we have worked under the Hele-Shaw model assumptions (which we outline more precisely in § 2.2). These assumptions and this style of modelling are however strictly valid for single-phase flows. For multi-phase systems a variety of phenomena can impact the validity of the model assumptions at the interface. In the first place, under suitable conditions on the mobility ratio, it is known that local instabilities arise, i.e. viscous fingering (see e.g. Homsy 1987). In the second place, dispersive effects are always present in a miscible displacement. Thirdly, the local velocity is always nearly three-dimensional at the interface.

The combination of the above three phenomena can be complex and their impact on the validity of the Hele-Shaw approach is subtle. Regarding viscous fingering, for the most part this is not a concern for the flows considered as we typically have positive viscosity ratios. Dispersive effects are present in our flows, in particular due to significant azimuthal current close to the interface, driven by annular eccentricity. These effects will form a significant part of our study. We note however that the experimental time scales considered are relatively short, meaning that we are very far from diffusive dispersion regimes. Regarding three-dimensional effects at the interface, these are unavoidable. As with dispersion, these effects are an inherent property of all real flows and cannot be eliminated by strategies such as working with small aspect ratios. Instead the key question is whether or not these local phenomena have an impact on the global dynamics of the system or whether the effects remain local, as is often the case. Zimmerman & Homsy (1991) found that the local details of the concentration front close to the interface were relatively unimportant in comparison to the bulk pressure gradients.

There is a growing literature on miscible displacements in pipes and channels. Whilst relevant, here we have strong geometric effects on the base flow, so that direct comparison with this literature is hard. Instead, we highlight within our results when we have observed similar effects to those already published.

An outline of our paper is as follows. In § 2 following, we describe the experimental set-up. The first sequence of results is given in § 3, where we classify the displacements as either steady or unsteady, in each of our six series of experiments. Section 4 examines the significant role of dispersion and secondary flows in our experiments, illustrating the various observed phenomena. We close with a discussion, comparing

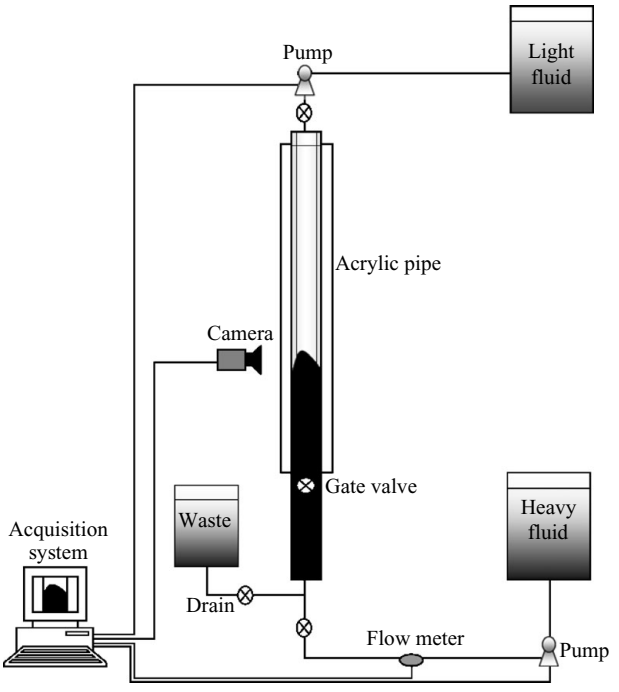

FIGURE 2. Schematic of the experimental set-up.

with model results and assessing the overall validity of the Hele-Shaw modelling approach.

2. Experimental methodology

A schematic of the experimental set-up is given in figure 2. The annulus dimensions are $\hat{r}_o = 1.91$ cm, $\hat{r}_i = 1.27$ cm and a length of 188.3 cm. The outer pipe is constructed from acrylic tubing with a wall thickness of 12.7 mm. The inner body is an aluminium pipe with wall thickness of 1.58 mm. It is mounted such that the position of the inner pipe can be adjusted relative to the fixed outer pipe to create the desired eccentricity. Eccentricity is measured by depth gauges mounted on either end of the annulus. The annulus is immersed in a tall tank with a square cross-section filled with glycerin to reduce optical distortion.

The flow loop consists of a progressive cavity pump (PCP) supplying the annulus with displacing fluid. The flow rate is controlled by a variable frequency drive. A thermocouple is mounted inside the inlet pipe of the annulus. The flow rate is measured with a Cole Parmer pilot-scale magnetic flowmeter (EM101-038) which the manufacturer specifies as accurate to 2 %, the output of which was directed to the control computer. The flowmeter's accuracy was checked in a simple calibration experiment by measuring the mass of fluid pumped over a fixed time interval.

To run a typical displacement experiment the upper section of the annulus is filled initially with displaced fluid while the gate valve is closed. Then, the bottom section of the annulus, below the gate valve, is filled with displacing fluid. A displacement experiment starts by slowly opening the gate valve and pumping the displacing fluid, dyed black, from the bottom of the annulus to the top (see figure 2). The fluids were dyed with ordinary (Higgins Eternal) pen ink, at a concentration of 300 p.p.m.

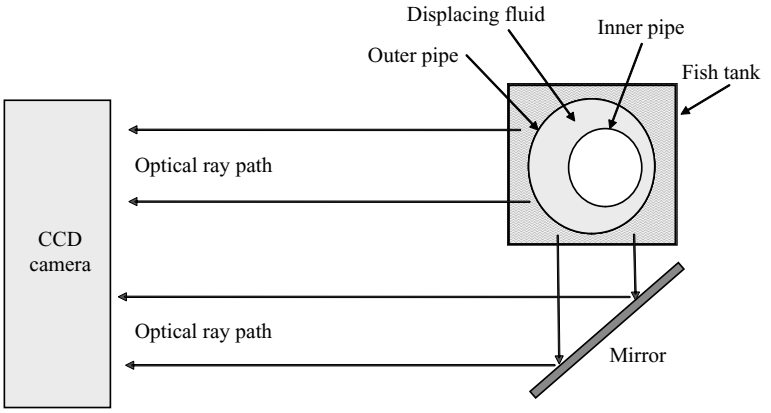

FIGURE 3. Schematic of the optical set-up.

Imaging of the interface occurred at two different axial positions, namely 300 mm and 1000 mm above the gate valve. A digital camera images 270° of the annulus by the use of a mirror (see figure 3). Each image thus consists of a reflected image from the side of the annulus and a non-reflected image from the front. Images are captured at a frame rate that depends on the flow rate, ranging from 10 Hz at high flow rates to 4 Hz at slow flows. The images are captured in uncompressed 8 bit monochrome format, with a signal to noise ratio of 50 dB. The two images are *unwrapped* via a simple geometric transformation. The edges are located on the transformed images, and then the two images are collocated and registered. Pixel values of the images were recorded along the circumference at these two heights. Pixel values varied in greyscale from 0 (white) to 255 (black), and a total of 130 pixels were located on each circumferential line. Before starting any analysis, an initial background image is subtracted from each image, to correct for local lighting variations. As the interface passes each fixed height, the value of each pixel on the circumferential line increases from zero until it reaches a maximum. This process at each pixel can be described by a saturation curve in which darkness intensity is plotted against time. By normalizing with the local maximum pixel value, the normalized darkness intensity varies from 0 to 1 as the interface passes. The saturation time, when an interface is regarded to have passed a given position is the time at which the normalized darkness intensity is equal to 0.95, i.e. because the *interface* is never completely sharp in a miscible displacement.

2.1. *Interface shape analysis*

In an ideal case where the interface is a horizontal line all pixels are saturated simultaneously. However in an eccentric annulus, a flat interface is rarely formed and pixels are saturated at different times. By subtracting the saturation time measured for pixel j at the upper (downstream) location from that at the lower (upstream) location, we arrive at a residence time $\Delta\hat{t}_j$, which is the time taken for the interface to traverse between lower and upper positions at the azimuthal position corresponding to pixel j.

On assuming a 'piston-like' displacement at the mean speed of the flow, say $\hat{w}^* = \hat{Q}/\pi(\hat{r}_o^2 - \hat{r}_i^2)$, the idealized mean residence time is denoted $\Delta\hat{t}_p$:

$$\Delta\hat{t}_p = \frac{\Delta\hat{y}}{\hat{w}^*}, \tag{2.1}$$

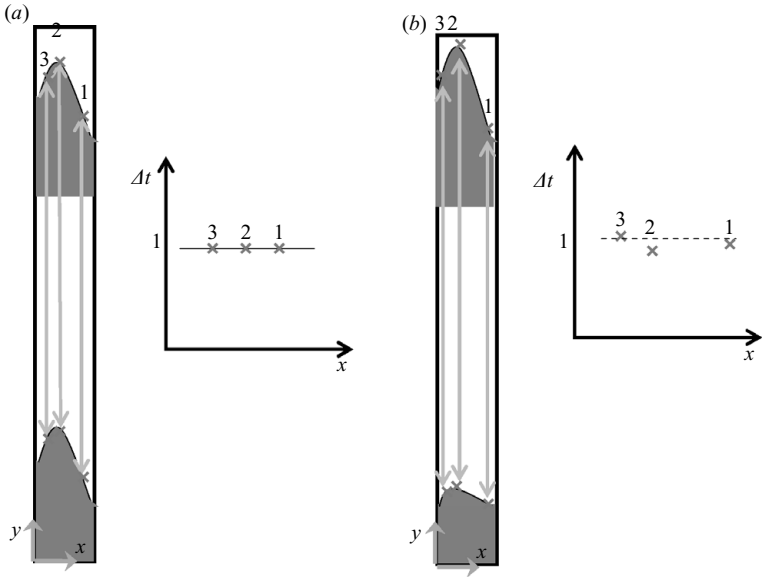

FIGURE 4. Schematic of interface shape and residence time variations for: (*a*) steady displacement (*b*) unsteady displacement. If all points lie on $\Delta t = 1$, they move at exactly the bulk mean velocity.

where $\Delta\hat{y} = 700\,\text{mm}$ is the vertical distance between upper and lower measurement locations. Throughout the paper we shall use the 'hat' notation, i.e. $\hat{\cdot}$, to denote variables that are dimensional. The piston-like residence time is used to scale the individual residence times, resulting in

$$\Delta t_j = \frac{\Delta\hat{t}_j}{\Delta\hat{t}_p}, \quad j = 1, 2, \ldots, 130. \tag{2.2}$$

In a steady displacement, where the interface travels in a steady manner, the normalized Δt_j should give the same constant value for each pixel j (see figure 4*a*). It should be noted that the interface itself does not need to be horizontal in order for Δt_j to be constant. The interface can be any shape so long as it maintains that shape during displacement.

In an unsteady displacement (see figure 4*b*), the fluid on the wide side flows faster than the fluid on the narrow side. Thus, the interface stretches as the flow progresses. Different pixels along the circumference have different residence times and the distribution of Δt_j suggests the unsteadiness of the displacement. For an objective measure of the unsteadiness we may consider the standard deviation of the Δt_j distribution, say $\sigma_{\Delta t}$. A large standard deviation (relative to the mean of Δt_j) suggests an unsteady displacement while a small standard deviation (relative to the mean of Δt_j) suggests a steady displacement.

2.2. *Experimental design and process related issues*

As explained in § 1 the objectives of our study were partly to provide a controlled set of annular displacement experiments, suitable for exploring the validity of the Hele-Shaw modelling approach adopted previously, and partly to consider displacements

in parameter ranges having some overlap with field conditions. We therefore briefly review the dimensionless parameters of relevance to the modelling approach and field conditions. For further detail on the modelling approach the reader is referred to Bittleston *et al.* (2002) or Pelipenko & Frigaard (2004*c*).

The main simplifications that we adopt, with respect to industrial conditions, are to consider a single uniform section of the annulus, fix the orientation at vertical and to consider only 2 fluids in our displacement. The fluid types that we consider are shear-thinning and yield stress fluids, although half of the experiments are conducted with Newtonian fluids. These fluids are characterized in the oilfield cementing industry by rheological models such as the Herschel–Bulkley model (including the Bingham, power law and Newtonian models as subcases). This model contains three parameters: the yield stress $\hat{\tau}_{k,Y}$, the consistency $\hat{\kappa}_k$ and the (shear-thinning or) power law index n_k (where $k = 1, 2$ denotes the fluid). The fluid densities are denoted $\hat{\rho}_k$.

In order to follow the Hele-Shaw approach of Bittleston *et al.* (2002), we define the aspect ratio of circumferential and radial length scales δ in the following way:

$$\delta = \frac{\hat{r}_o - \hat{r}_i}{\pi(\hat{r}_o + \hat{r}_i)}. \tag{2.3}$$

Azimuthal and axial distances are scaled with $0.5\pi(\hat{r}_o + \hat{r}_i)$, whereas radial distance from the annular centreline is scaled with $0.5(\hat{r}_o - \hat{r}_i)$. For a velocity scale we take the mean flow velocity $\hat{w}^*$:

$$\hat{w}^* = \frac{\hat{Q}^*}{\pi\left(\hat{r}_o^2 - \hat{r}_i^2\right)}. \tag{2.4}$$

Axial and azimuthal velocity components are scaled with $\hat{w}^*$, and radial velocity with $\delta\hat{w}^*$. A representative shear rate is $\hat{\dot{\gamma}}^* = 2\hat{w}^*/(\hat{r}_o - \hat{r}_i)$, which is used for the viscous stress scale $\hat{\tau}^*$:

$$\hat{\tau}^* = \max_{k=1,2}[\hat{\tau}_{k,Y} + \hat{\kappa}_k(\hat{\dot{\gamma}}^*)^{n_k}]. \tag{2.5}$$

The viscosity scale is $\hat{\mu}^* = \hat{\tau}^*/\hat{\dot{\gamma}}^*$, and finally, densities are scaled with the maximum density: $\hat{\rho}^* = \max_{k=1,2}\{\hat{\rho}_k\}$.

Primarily the Hele-Shaw approach relies on the neglect of terms in the Navier–Stokes equations that are of $O(\delta)$ and $O(\delta Re)$, where

$$Re = \frac{0.5(\hat{r}_o - \hat{r}_i)\hat{w}^*\hat{\rho}^*}{\hat{\mu}^*} \tag{2.6}$$

is the Reynolds number. The field range for δ is typically in the range 0.01–0.1. Our annular radii give $\delta = 0.064$, which is in this range. We have also conducted a limited number of experiments in a slightly larger aspect ratio annulus, $\delta = 0.084$. Moving to a much narrower annular gap presents problems in both cleaning of the apparatus and in terms of controlling the uniformity when eccentric, i.e. small deflections of the inner or outer wall become very significant. Regarding the Reynolds number, this has a very wide range in field applications, ranging from near-creeping flows to strongly turbulent flows. However, for very large Re flows the Hele-Shaw approach is anyway not applicable, so here we focus mainly on experimental laminar flows in the Reynolds number range of 0–10. This is restrictive from the industrial perspective but does represent a limiting parameter regime that is easier to understand.

There are two development lengths to consider in our apparatus. Firstly, we have a development length scale associated with the width of the annular gap. The time

scale for viscous diffusion across the annular gap is

$$\hat{t}_v = \frac{\hat{\rho}^*(\hat{r}_o - \hat{r}_i)^2}{4\hat{\mu}^*} \tag{2.7}$$

and the length scale is thus: $\hat{w}^*\hat{t}_v \ll 0.5\pi(\hat{r}_o + \hat{r}_i) \approx 5\,\text{cm}$, since we have $\delta Re \ll 1$ for the flows considered. Secondly, we may consider development of the Hele-Shaw type flow in the azimuthal-axial directions. The boundaries at the ends of the Hele-Shaw cell (annulus) are fully mobile and there are no fixed boundaries in the azimuthal direction to generate boundary layer flows. Therefore, we expect flow developments to take place on the shortest length scale of the Hele-Shaw cell, i.e. the azimuthal length scale: $0.5\pi(\hat{r}_o + \hat{r}_i)$. For steady displacements another development length relates the length required for the front and rear of the interface to pass the entry point. At the inflow, there is also a development from the initial shape of the interface at the gate valve towards a steady state shape. Typical steady displacements we have observed experimentally in vertical annuli do not have axial extensions greater than the azimuthal length scale $0.5\pi(\hat{r}_o + \hat{r}_i)$. Thus, it appears that the choice of lower observation point at 30 cm is reasonable.

Other than the Reynolds number, which does not appear in reduced models, the main flow-controlling parameter is the dimensionless buoyancy number. $b = (\rho_2 - \rho_1)/St^*$. Here St^* is the Stokes number of the flow, defined in terms of the dimensional parameters by

$$St^* = \frac{\hat{\tau}^*}{0.5\hat{\rho}^*\hat{g}(\hat{r}_o - \hat{r}_i)}. \tag{2.8}$$

The Stokes number can vary in the range 0.1–100 in the field setting, but the dimensionless density difference $(\rho_2 - \rho_1)$ is also small. In terms of dimensional quantities the buoyancy parameter b is defined by

$$b = \frac{0.5[\hat{\rho}_2 - \hat{\rho}_1]\hat{g}(\hat{r}_o - \hat{r}_i)}{\hat{\tau}^*}, \tag{2.9}$$

which clearly reflects the balance between buoyant and viscous stresses. Typical sizes of b may range from 0 to 10, and typically the displacing fluid is denser, meaning $b < 0$. Intuitively, we expect that $|b| \gg 1$ indicates the dominance of buoyancy over viscous effects.

With respect to the dimensionless geometric parameters in the flow, having fixed the inclination at vertical, the only other geometric parameter is the eccentricity e, defined as the distance between centres of the two cylinders, divided by the difference in radii. Although in strongly inclined wells values of e close to 1 do occur, in vertical wells this is rarer. A more common range would be $e \in [0, 0.6]$, which we can adequately cover. A practical difficulty with larger eccentricities (experimentally) is mentioned earlier in the context of smaller δ, i.e. small imprecisions in the apparatus geometry become significant with respect to the annular gap size, on the narrow side of the annulus.

In the modelling approach that we seek to validate, apart from b and e all other dimensionless parameters are rheological. For fluid k, the dimensionless rheological parameters are defined in terms of their dimensional analogues by

$$\kappa_k = \frac{\hat{\kappa}_k\left(\hat{\dot{\gamma}}^*\right)^{n_k}}{\hat{\tau}^*}, \quad \tau_{k,Y} = \frac{\hat{\tau}_{k,Y}}{\hat{\tau}^*}. \tag{2.10}$$

In the case that the fluids are Newtonian, note that the consistency is simply the viscosity.

In a field setting, power law indices in the range 0.3–1 are fairly commonplace, effective viscosities when sheared are 1–2 orders of magnitude larger than water. Yield stresses can range from 0 to 20 Pa. The Bingham number $B_k = \tau_{k,Y}/\kappa_k$, gives an indication of how plug-like the local velocity profile is, when viewed across the annular gap. A typical range is 0–10. It is worth commenting that at large values of Bingham number the flow is likely to become locally stationary on the narrow side of the annulus.

2.3. *Selection of fluids*

Although ideally one would like to be able to select fluids to match given dimensionless parameter ranges, in reality this is very difficult, and particularly as we wish to work with transparent and relatively inelastic fluids. The easiest parameter to vary experimentally between experiments is the flow rate. For Newtonian fluids, a change in the flow rate affects only b. Therefore, we may select a given fluid pair with desired viscosity ratio and fixed densities, then explore the space (e, b).

This was the approach adopted for the first three series of experiments, using glycerol solutions as a Newtonian fluid. Glycerol solutions were prepared by diluting pure glycerol with water. Density and viscosity of glycerol solutions are very sensitive to water content and temperature. Fluid densities were measured with a hydrometer, accurate to $\pm 1\,\mathrm{kg\,m^{-3}}$. Viscosities of fluids were tested before each experiment to check the self-consistency of experiments in each series.

For our non-Newtonian experiments Xanthan gum and Carbopol 940 were used. These fluids are complex long-chained polymers and were mixed according to the manufacturers' methodology. Rheology measurements showed that the effect of dye on the rheology of either fluid was insignificant. The rheological properties of each solution were determined using a Bohlin C-VOR digital controlled shear stress-shear rate rheometer. The temperature was fixed to be isothermal at a temperature of approximately 23 °C. The Xanthan measurements were highly repeatable, with an error of less than 2 % between successive measurements. The data were fitted to a power law model:

$$\hat{\tau} = \hat{\kappa}\hat{\dot{\gamma}}^{n}, \tag{2.11}$$

which is known to give a reasonable representation of the flow curve data, over a restricted range of shear rates.

Carbopol 940 was more challenging to characterize. It was found to exhibit thixotropic properties due to aging and polymer restructuring. In order to 'reset' the structure of the polymer between samples, all tests were subjected to a pre-shear of 30 s in the rheometer before data acquisition. This greatly improved repeatability especially at low shear rates. After pre-shearing, the stress values were acquired by the rheometer for an increasing ramp of shear rates. The rheological parameters of the fluids were determined by analysing the flowcurve data and fitting to a Herschel–Bulkley model.

$$\hat{\tau} = \hat{\tau}_Y + \hat{\kappa}\hat{\dot{\gamma}}^{n}. \tag{2.12}$$

The yield stress was determined finding the shear stress value at the global maximum of the viscosity. Once the yield stress was found, this value was subtracted from the remaining data, which was then fitted to a power law curve. The error on the parameter fitting is larger with Carbopol, particularly with regards to the yield stress, which can have an error, in the worst case, in the range 20–50 % since the global

	Displacing fluid (1)					Displaced fluid (2)				
Series	Fluid	Additive	$\hat{\rho}_1$ (kg m^{-3})	$\hat{\kappa}_1$ (Pa s^n)	n_1	Fluid	$\hat{\rho}_2$ (kg m^{-3})	$\hat{\tau}_Y$ (Pa)	$\hat{\kappa}_2$ (Pa s^n)	n_2
1	78 % Gly	0.4 % Salt	1200	0.049	1	78 % Gly	1192	–	0.049	1
2	88 % Gly	–	1234	0.15	1	78 % Gly	1192	–	0.049	1
3	98 % Gly	–	1254	0.64	1	78 % Gly	1192	–	0.049	1
4	0.3 % Xan	30 % Sug	1118	1.45	0.38	0.38 % Xan	1000	–	1.00	0.38
5	0.8 % Xan	–	1000	3.6	0.3	0.1 % Car	1000	2	2.2	0.3
6	0.3 % Xan	33 % Sug	1048	0.32	0.51	0.07 % Car	1000	0.6	0.91	0.36

TABLE 1. Fluids and properties in the experimental series. The percentages in this case refer to a wt/wt measure. A legend for the chemicals used is as follows: Salt is NaCl; Sug is sugar; Gly is glycerin; Xan is Xanthan gum and Car is Carbopol-940.

maximum is often not well defined. This apparently large error in $\hat{\tau}_Y$ has a relatively small impact on model usage for flowing fluids as the uncertainty occurs at very small strain rates. Once the yield stress is fixed, the fitting error is below 3.5 % for the consistency $\hat{\kappa}$ and 4 % for the power law index n.

2.4. *Experimental plan*

We aimed to study the effects on the displacement flows of variations in the dimensionless governing parameters of the Hele-Shaw model. Six series of experiments with Newtonian and non-Newtonian fluids were performed. Each experimental series corresponded to a fixed pair of fluids with the displacement performed at a range of different eccentricities and flow rates. The flow rate ranges were selected to maintain comparable ranges of $|b|$ (between 0 and 6.3) for each series. The fluids used and their physical properties are listed in table 1.

For the Newtonian–Newtonian displacements (series 1–3), the viscous stress scale is unaffected by the flow rate, which acts only on the buoyancy number. Glycerol solutions were used, at different concentrations in each series, to control the viscosity ratio. For the non-Newtonian fluids, we attempted to match the power-law indices of the two fluids (series 4 and 5). In this case the stress scale also changes with the nth power of the flow rate. This maintains a constant ratio of κ_1/κ_2, in the case of two power law fluids. Series 4 consisted of two different Xanthan solutions of the same power law index, but with a density and consistency difference. In series 5 we have looked at displacing Carbopol with Xanthan in the absence of a density difference (but with identical power law indices). Finally, series 6 considered displacing Carbopol with Xanthan in the presence of a density difference. Table 2 summarizes the experimental conditions for each series of experiments.

3. Experimental results

3.1. *Illustrations of typical displacements*

Before presenting parametric results from each series of experiments, we illustrate typical experimental results in the cases when a displacement is steady or unsteady. We commence by showing in figure 5 typical images from both a steady and unsteady displacement. Front and side images are presented at a sequence of different times, at lower and upper vertical positions. The first observation we make is that, although miscible, the bulk of the two fluids remains separate and unmixed. The interface itself

Series	Flow rate (L min^{-1})	e	$\lvert b\rvert$	κ_1/κ_2
1	0.17–0.72	0–0.5	0.9–3.7	1
2	0.17–0.72	0–0.5	1.5–6.3	3.1
3	0.17–0.72	0–0.5	0.5–2.2	13.1
4	0.17–0.72	0–0.5	1.2–2.2	1.45
5	0.17–0.72	0–0.5	0	1.6
6	0.10–2.16	0–0.5	0.7–1.4	0.37–0.46

TABLE 2. Experimental condition for the different series.

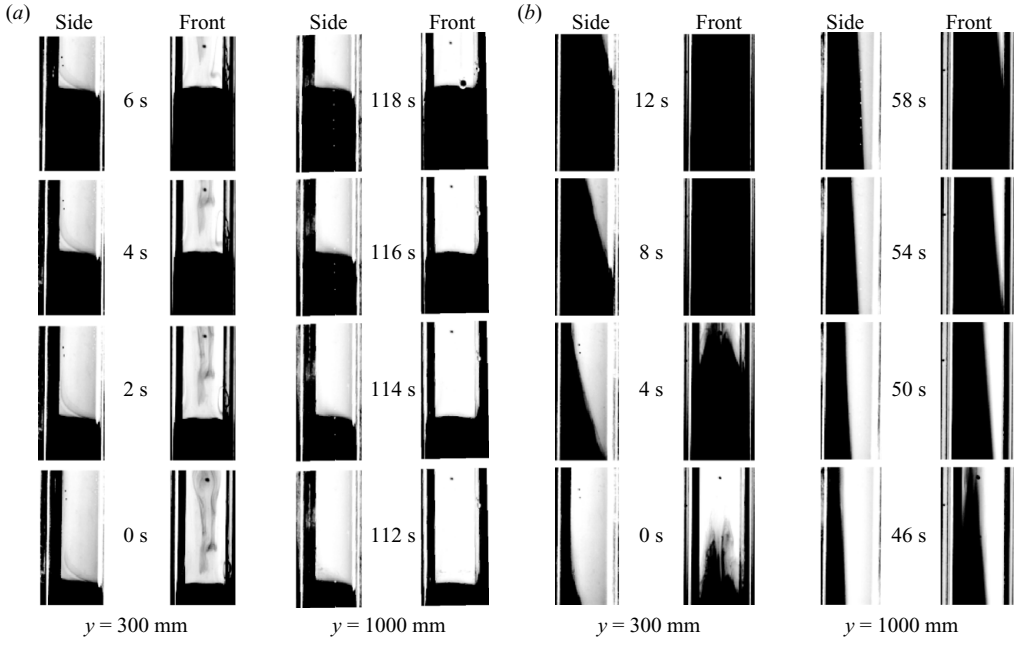

FIGURE 5. Examples of steady and unsteady displacements: (*a*) $e = 0.5$, $\hat{Q} = 0.17\,\mathrm{L\,min^{-1}}$, fluid properties from series 3; (*b*) $e = 0.2$, $\hat{Q} = 0.34\,\mathrm{L\,min^{-1}}$, fluid properties from series 1. In each of (*a*) and (*b*) the left two columns of the figures shows successive time frames at the lower (upstream) position, $y = 300\,\mathrm{mm}$ (front and side views), whereas the last two columns show images at the upper (downstream) vertical position, $y = 1000\,\mathrm{mm}$ (front and side views). The zero reference time is at the start of the first image.

is somewhat diffused and we can observe dispersive currents within the flow, but there is no large-scale mixing in evidence. Qualitatively, the shape of the interface in figure 5(*a*) translates axially while remaining constant, whereas that in figure 5(*b*) elongates progressively. To see the elongation more clearly compare the slope of the interface in the side views, at lower and upper positions. Due to background lighting variations these images are obscured to the left of the side views, but once the background light is subtracted, the darkness intensity data is much clearer.

To quantify more precisely this notion of steady/unsteady displacement and to measure the amount of dispersion, we construct spatio-temporal plots at the upstream

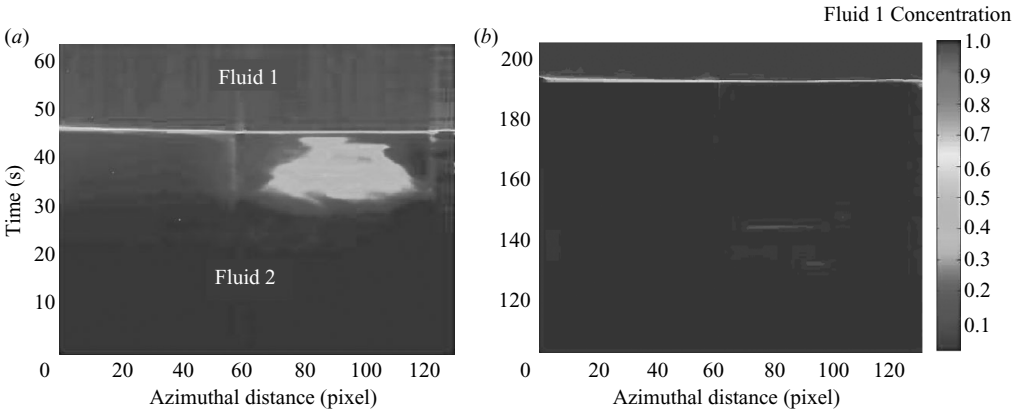

FIGURE 6. Spatio-temporal for the displacement of Figure 5(*a*): (*a*) upstream location; (*b*) downstream location.

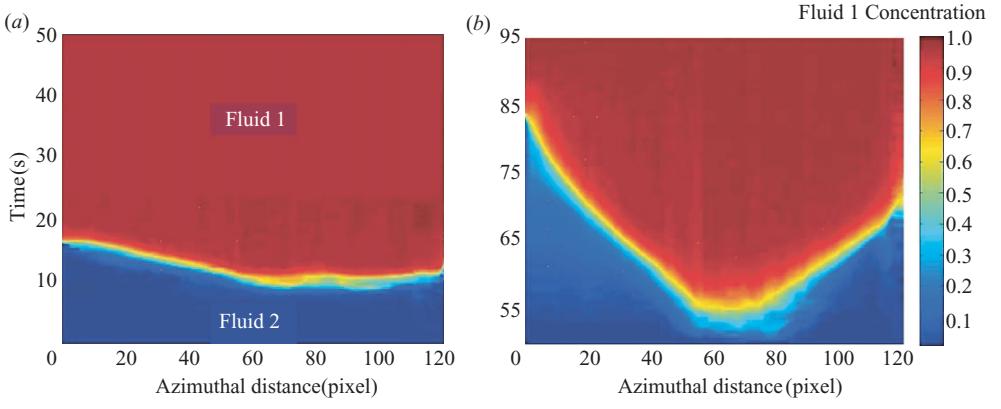

FIGURE 7. Spatio-temporal for the displacement of Figure 5(*b*): (*a*) upstream location; (*b*) downstream location.

and downstream locations, using the normalized darkness intensity. These are shown in figures 6 and 7, for the experiments reported in figures 5(*a*) and 5(*b*) respectively. The azimuthal distance shown corresponds to roughly 3/4 of the annulus. The left-hand side corresponds to the narrow side of the annulus. The x-axis is measured in pixels, with the first 65 pixels coming from the side view and the last 65 from the frontal view.

In figure 6 we observe at initial times that the cross-section is full of fluid 2. We see a large diffuse cloud of intermediate colour scale emerging at around $\hat{t} = 20\,\mathrm{s}$. This effect comes from opening of the gate valve, which entrains fluid 1 into fluid 2 as can be observed in the images of figure 5(*a*) at the upstream (lower) position. Other than this effect, we observe that the temporal frontier between fluids 1 and 2 remains horizontal with a very small azimuthal variation in these figures. In fact the interface at the upper position appears flatter than that at the lower position, since the entrainment effects of valve opening have dissipated further downstream. By comparison with figure 6, the spatio-temporal plot for the unsteady displacement (figure 7) shows strong azimuthal variations at both lower and upper positions. The

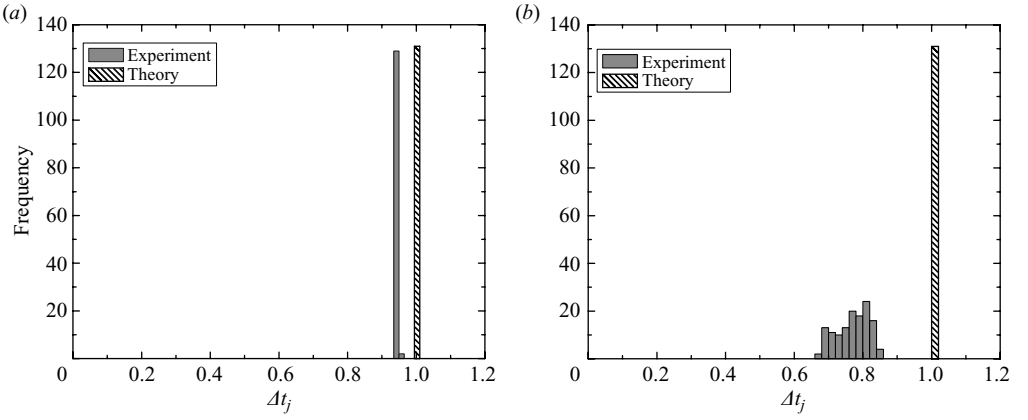

FIGURE 8. Residence time distribution for the displacements of figures 5(*a*) and 5(*b*), respectively. (*a*) $\mu_{\Delta t} = 0.95$, $\sigma_{\Delta t}/\mu_{\Delta t} = 0.0026$; (*b*) $\mu_{\Delta t} = 0.77$, $\sigma_{\Delta t}/\mu_{\Delta t} = 0.06$.

arrival times at the upper location are much shorter at the wide side than at the narrow side. We again have some localized entrainment and mixing at the lower position, just after the gate valve is opened.

3.2. *Parametric results: Newtonian fluids*

We now present the results of our different series of experiments, in particular focusing on the question of whether the displacement may be considered steady or unsteady. In order to make this type of classification, we need to have a meaningful measure of the unsteadiness. Using the method explained in § 2.1 we compute the scaled residence times Δt_j at each pixel value j, i.e. the time taken for the interface to pass from upstream to downstream measurement locations, divided by the mean theoretical time of travel as computed from the flow rate. Typical frequency distributions of residence times are shown in figure 8 for the displacements of figures 5(*a*) and 5(*b*).

Evidently, the standard deviation of the residence time distribution $\sigma_{\Delta t}$ is much smaller for the displacement of figure 5(*a*) than for that of figure 5(*b*). Perhaps a less obvious effect is that the mean residence time $\mu_{\Delta t}$ of the displacement of figure 5(*a*) is significantly larger than that of figure 5(*b*), but is still less than unity. This effect is due to dispersive fluid currents, which we shall discuss at length later.

For all steady displacements we have systematically found $\mu_{\Delta t} < 1$, which discounts the possibility of a random experimental error. We have carried out some concentric test displacements in which glycerol displaces air, where dispersion is minimal and still $|\mu_{\Delta t} - 1| \approx 0.02$, which is some measure of the imperfection of our apparatus. There are also more random errors due to pump flow rate fluctuations, geometrical imperfections, image processing, etc., which ensure that $\sigma_{\Delta t} > 0$. The size of these errors is indicated by the value of $\sigma_{\Delta t}/\mu_{\Delta t}$, when measured in steady displacements, and is typically $< 1\,\%$.

For each experimental series we use $\sigma_{\Delta t}/\mu_{\Delta t}$ to compare between experiments, as e and $|b| = -b$ are varied. In figure 9(*a–c*) we present the values of $\sigma_{\Delta t}/\mu_{\Delta t}$ for each of series 1–3, respectively. The experimental values are also used to construct the shaded contour plots using two-dimensional linear interpolation and extrapolation. Given that the matrix of experimental points in each series remains fairly sparse, we interpret these contours mostly as a qualitative indication of the variation of $\sigma_{\Delta t}/\mu_{\Delta t}$, except close to each data point. In particular, the extrapolation to $|b| = 0$, outside of

the range of experimental $|b|$, appears non-physical in figure 9(c), but otherwise is at least consistent with our physical intuition. By comparison between figure 9(a–c), we observe that increasing the viscosity ratio has the effect of reducing $\sigma_{\Delta t}/\mu_{\Delta t}$, i.e. stabilizing the flow and promoting steadiness. Increasingly steady displacements are also found for less eccentric annuli and larger buoyancy $|b|$.

We have also classified each experimental displacement as either steady (squares) or unsteady (triangles). Figure 9(d) shows a typical variation of $\sigma_{\Delta t}/\mu_{\Delta t}$ as b is varied. In a regime which is categorized as steady there is very little variation in $\sigma_{\Delta t}/\mu_{\Delta t}$, about some small constant value. However, we consistently observe a rapid change in $\sigma_{\Delta t}/\mu_{\Delta t}$ as $|b|$ is decreased and the interface becomes unsteady. We classify by identifying this rapid change in $\sigma_{\Delta t}/\mu_{\Delta t}$ with b at each fixed e. It is not possible to specify an exact and universal transition threshold. This notion is anyway problematic since some dispersion is always present and the amount is fixed. However, typically we have recorded values $\sigma_{\Delta t}/\mu_{\Delta t} \lesssim 1\,\%$ before the transition to unsteadiness, and displacements become obviously unsteady for $\sigma_{\Delta t}/\mu_{\Delta t}$ in the range 3 %–5 %.

For series 1 (figure 9a) both fluids have the same viscosity and the displaced fluid is less than 1 % lighter than the displacing fluid. Steady displacement was only achievable in the concentric annulus or at small eccentricity with very low flow rate. In series 2 (figure 9b), the displacing fluid is three times more viscous than the displaced fluid and is 3.5 % denser than the displaced fluid. Although the density difference was very small, steady displacement were achieved even at high eccentricities with sufficiently low flow rates, $|b| > 3$. In series 3, with larger viscosity ratio, steady displacements were found at smaller values of $|b|$. Over the ranges of fluid properties and flow rates tested it appears that the buoyancy stress versus viscous stress balance, captured in b, has a more significant stabilizing effect than viscosity ratio alone.

3.3. *Parametric results: non-Newtonian fluids*

Three series of experiments were conducted with non-Newtonian fluids using Xanthan gum and Carbopol 940 solutions. In the first series of non-Newtonian experiments (figure 10a), a power law fluid displaced another power law fluid with lower consistency. It should be noted that both fluids have the same power law index so that the effects of shear thinning, as the flow rate is increased, are similar in both fluids and the dimensionless ratio κ_1/κ_2 also remains invariant as the flow rate changes. In figure 10(a) the contours show the same qualitative trends as for the Newtonian displacements. A little buoyancy is required to make displacements steady when there is some eccentricity.

In the second series of non-Newtonian displacement experiments, a viscoplastic fluid (Carbopol) was displaced by a power law fluid (Xanthan). Again by matching the power law indices, the effects of shear thinning in each fluid are broadly similar. In this series of experiments, the fluids were of the same density ($|b| = 0$), the displacing fluid had a larger consistency value, but no yield stress. Steady displacement of the Carbopol was never achieved even at $e = 0$. Long static channels of Carbopol were observed on the narrow side of the annulus for $e > 0.1$. Due to the extensive channelling it was not possible to quantify $\sigma_{\Delta t}/\mu_{\Delta t}$.

In the last series of non-Newtonian experiments, by adding 5 % density difference to the displacing fluid, steady displacements resulted in both eccentric and concentric annuli (see figure 10b). Although the displacing fluid has a smaller consistency than the displaced fluid, the density difference is sufficient to displace the yield stress fluid from the narrow side of the annulus.

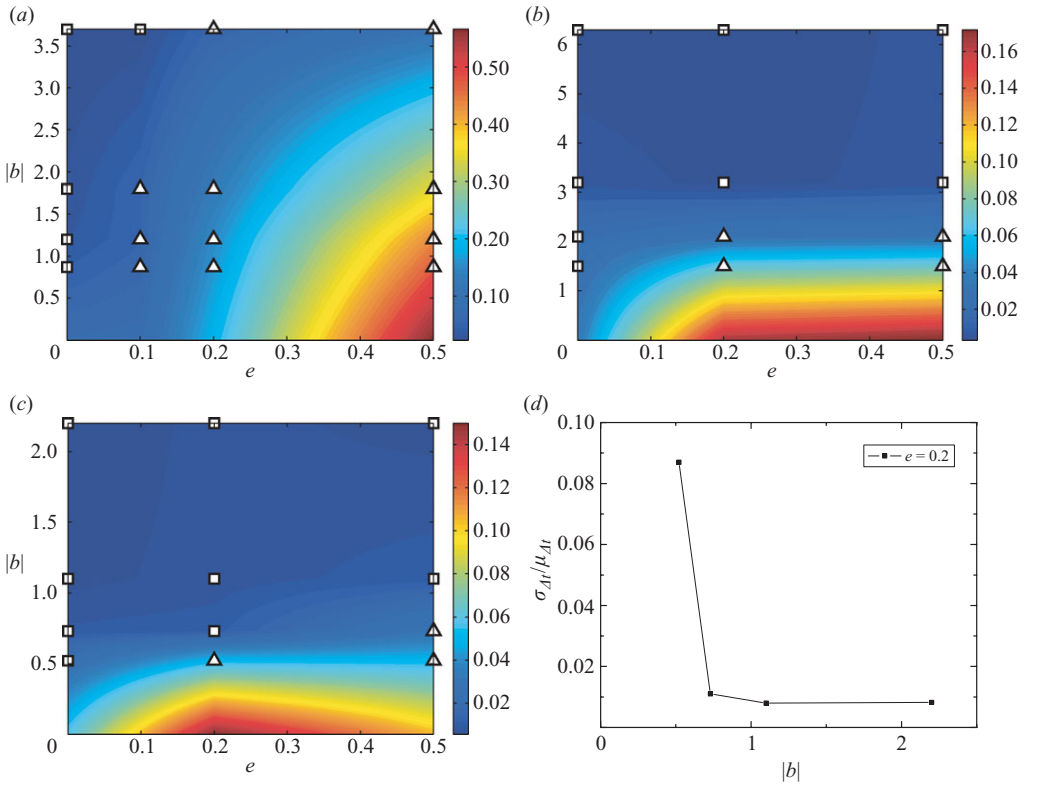

FIGURE 9. Variation of $\sigma_{\Delta t}/\mu_{\Delta t}$ for Newtonian fluid series 1–3: (*a*) series 1 ($\kappa_1/\kappa_2 = 1$); (*b*) series 2 ($\kappa_1/\kappa_2 = 3.1$; (*c*) series 3 ($\kappa_1/\kappa_2 = 13.1$). The contour plots are constructed from interpolation and extrapolation and each experimental point is classified as either steady (squares) or unsteady (triangles). In (*d*) we show a typical variation in $\sigma_{\Delta t}/\mu_{\Delta t}$ with $|b|$ for $e = 0.2$, from series 3.

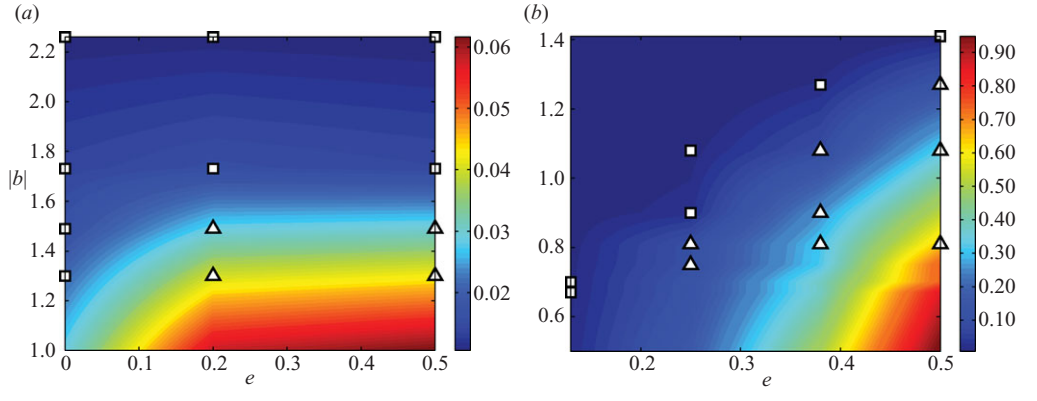

FIGURE 10. Variation of $\sigma_{\Delta t}/\mu_{\Delta t}$ for non-Newtonian fluid series: (*a*) series 4 (power law fluid displacing power law fluid, Xanthan–Xanthan); (*b*) series 6 (power law fluid displacing visco-plastic fluid, Xanthan–Carbopol).

4. Secondary flows and dispersion

It is immediately apparent when observing these displacement flows that a number of secondary phenomena influence the flow. These fluids are miscible, but the time

scale of the experiments ($\sim$100 s) is very much shorter than that for molecular diffusion. Thus, many of the observed effects are essentially dispersive and we use this terminology to loosely describe these phenomena. Note, however, that we are also parametrically far from the laminar Taylor dispersion regime, so that the effects observed are local and not averaged by cross-gap dispersion in any way.

4.1. *Radial effects: dispersion on the scale of the annular gap*

To start with, if we consider the idealization of the narrow annular gap as a plane channel, along which we are displacing vertically upwards, we expect to see a displacement finger advance in the centre of the channel faster than the mean flow. This type of symmetric duct displacement flow has been studied in some depth, in both tubes and plane channels, experimentally by Petitjeans & Maxworthy (1996), Lajeunesse *et al.* (1997, 1999, 2001), Lajeunesse (1999), Scoffoni, Lajeunesse & Homsy (2001), Gabard (2001) and Gabard & Hulin (2003), and computationally by Chen & Meiburg (1996), Rakotomalala, Salin & Watzky (1997), Yang & Yortsos (1997), Allouche, Frigaard & Sona (2000), Frigaard, Scherzer & Sona (2001), Zhang & Frigaard (2006), Goyal & Meiburg (2006, 2007), Schafroth, Goyal & Meiburg (2007) and Vanaparthy & Meiburg (2008). Both Newtonian and non-Newtonian fluids have been considered.

Since we deal primarily with 'stable' viscosity ratios, $\kappa_1 > \kappa_2$, as is common in the industrial setting, the advancing displacement finger is expected to be locally stable, i.e. this is not a viscous finger. This may be thought of as a form of dispersion in which the dispersive effects are modulated by the positive viscosity ratio, $\kappa_1 > \kappa_2$ and possibly by buoyancy $b < 0$, both of which act via modifying the velocity field of the underlying Poiseuille flow, close to the interface. Amongst locally stable displacements, dispersive effects are most prominent when the two fluids are identical. An example of such a displacement is shown in figure 11, taken from a Newtonian experiment in the larger aspect ratio annulus, $\delta = 0.084$, which aids visualization. The fluids are identical, except for the colouring of the displacing fluid. The annulus is eccentric, $e = 0.25$, and therefore we observe the finger advancing first on the wide side of the annulus (figure 11*a*). As the displacement advances, in figure 11(*c*) we first see the front on the narrow side. Optically we do not see this as a finger since the displacing fluid finger at other azimuthal positions partly masks the interface. At later times we observe near-complete displacement with thinning residual wall layers.

In the case just examined, taking the analogy of the plane channel flow, we would expect the tip of the displacement front to advance at 1.5 times the mean flow, as the interface is simply advected by the plane Poiseuille velocity profile. For two identical power law or Herschel–Bulkley fluids this same ratio may be easily calculated, and is reduced due to both shear-thinning and yield stress effects. When the fluids are not identical, some idea of the front speed at the channel centre can be gained from a lubrication/thin-film style of model. Such models have been developed by Lajeunesse *et al.* (1999) for the case of two Newtonian fluids and by Allouche *et al.* (2000) for two Bingham fluids. These models give qualitative information concerning the effects of rheological and buoyancy parameters, but do also overpredict the front speed as they ignore the multi-dimensional nature of the flow at the front.

We have developed such a model for two Herschel–Bulkley fluids (i.e. including Newtonian and power-law models), with a density difference, and have run various exploratory computations. In general and as might be expected, for stable viscosity ratios and moderate buoyancy number, the front velocity versus mean velocity ratios lie between 1 and that of the identical fluid case. It is only for dimensionless parameters

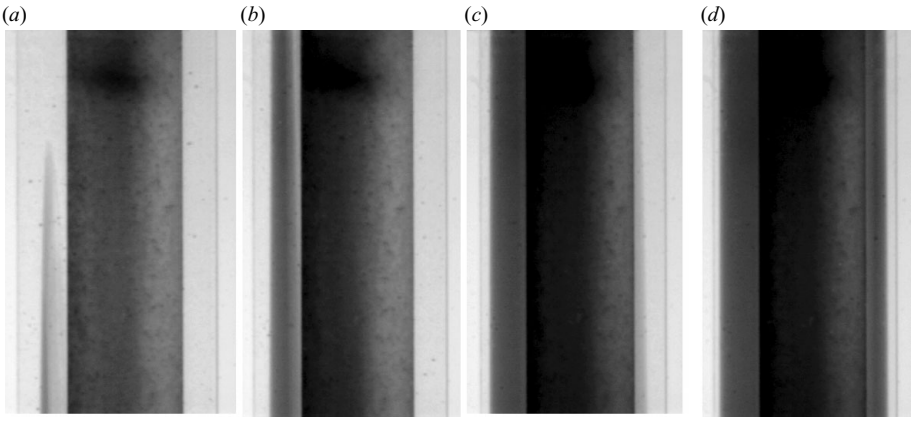

FIGURE 11. Dispersive finger in the displacement flow of two identical Newtonian fluids: $\hat{\kappa}_1 = \hat{\kappa}_2 = 0.31$ Pa.s: (*a*) $\hat{t} = 0$ s; (*b*) $\hat{t} = 4.1$ s; (*c*) $\hat{t} = 16$ s; (*d*) $\hat{t} = 32$ s. The annular eccentricity is $e = 0.25$ and the aspect ratio $\delta = 0.084$.

that are more extreme than those considered in our experiments that the centreline front velocity approaches close to 1, with ratios in the range 1.15–1.5 being more common. If this type of gap-scale dispersion was acting alone in an unmodified fashion, we would be observing residence times smaller than those typically observed for steady displacements. For example, in the context of the steady displacements of series 1–3 (figure 9*a–c*), the mean scaled residence times are of the order of $0.95 \approx 1/1.05$.

4.2. *Azimuthal effects: large-scale dispersion driven by circumferential flows*

As discussed above, it is likely that gap-scale dispersion effects are modified by other secondary flows present in the annulus. That such secondary flows exist has been known for many years (see e.g. Tehrani *et al.* 1993; Bittleston *et al.* 2002; Pelipenko & Frigaard 2004*a*). Indeed, in the case of a steady displacement in an eccentric annulus, there can be no stable steady front without azimuthal secondary flows.

To illustrate the effects of these azimuthal currents we present a short series of result from the large aspect ratio annulus, $\delta = 0.084$ (in which dispersive effects are amplified). For this series the displaced fluid 2 was a white corn syrup (Crown brand) and the displacing fluid 1 was an undiluted gold corn syrup. The density difference was varied by diluting the mixture by 8 % with a 20 % salt solution to fluid 2, resulting in densities: $\hat{\rho}_1 = 1398\,\mathrm{kg\,m^{-3}}$ and $\hat{\rho}_2 = 1363\,\mathrm{kg\,m^{-3}}$. The viscosities were $\hat{\kappa}_1 = 6.24$ Pa.s and $\hat{\kappa}_2 = 0.76$ Pa.s. In the three experiments shown, the flow rate $\hat{Q}$ was increased: $\hat{Q} = 3 \times 10^{-6},\ 6 \times 10^{-6},\ 12 \times 10^{-6}$. The annulus had eccentricity, $e = 0.25$. This resulted in the following set of dimensionless numbers: $\kappa_1 = 1$, $\kappa_2 = 0.122$, and $-b = 0.222,\ 0.111,\ 0.056$, for the three increasing flow rates.

First we present results from the Hele-Shaw model of Pelipenko & Frigaard (2004*b*), shown in figure 12(*a–c*). Each figure shows the interface and the moving frame stream lines at a dimensionless time, $t = 10$, by which time the displacement is in steady state. Each figure shows only half of the annulus, with the wide side at $\phi = 0$ and the narrow side at $\phi = 1$. Moving left to right in this figure the flow rate increases, hence $|b|$ decreases. These are the streamlines relative to the mean velocity. The counter-current secondary flow is evident: from wide to narrow side under the interface and from narrow to wide side above the interface. To explore the effect of eccentricity,

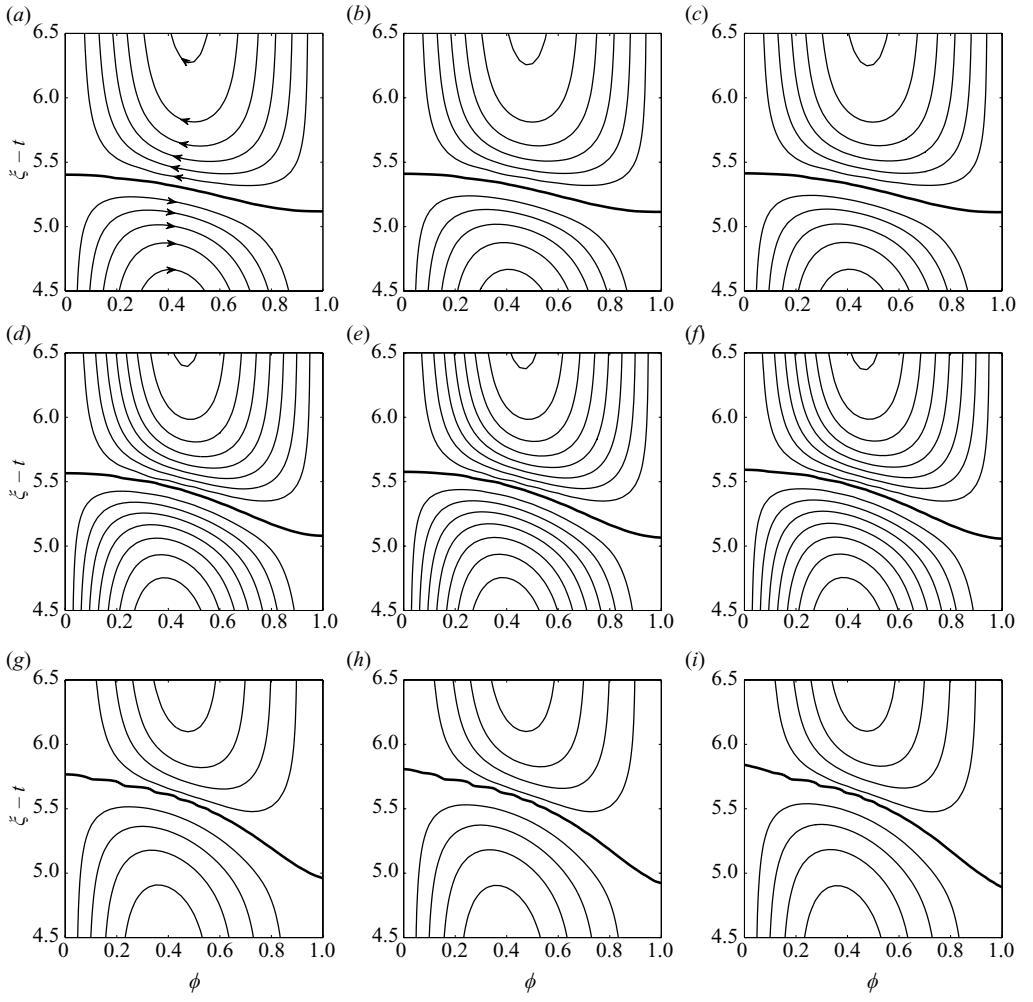

FIGURE 12. Moving frame streamlines and interface (heavy line) computed from the model of Pelipenko & Frigaard (2004*b*), at time $t = 10$, for two Newtonian fluids with $\kappa_1 = 1$, $\kappa_2 = 0.122$: (*a–c*) $e = 0.25$ with $b = -0.222, -0.111, -0.056$, respectively; (*d–f*) $e = 0.38$ with $b = -0.222, -0.111, -0.056$, respectively; (*g–i*) $e = 0.5$ with $b = -0.222, -0.111, -0.056$, respectively. Contour spacing for the moving frame streamlines is at intervals 0.02 for (*a–f*), and at 0.04 for (*g–i*). Direction of circulation as indicated in (*a*).

we also present in figure 12(*d–i*), equivalent results at an eccentricity of 0.38 and 0.5, with the same fixed values of b. The strength of the secondary flow increases in line with the eccentricity, as suggested by the argument outlined above. In each figure the direction of circulation of the fluids follows that indicated in figure 12(*a*).

Figure 13 shows the experimental results corresponding to figure 12(*a–c*). The figure shows snapshots of the displacement front and below it are the results of an edge detection algorithm, with five interfaces imaged at increasing distance along the annulus. By comparison with figure 12(*a–c*), it is immediately apparent that there are some significant differences. At this large viscosity ratio, the interfaces are stable and the displacements all appear steady. As $|b|$ decreases however, the effects on the model results are minimal, but very noticeable in the experiment. Smaller $|b|$ corresponds to larger flow rate and the size of the secondary azimuthal flows scale in proportion

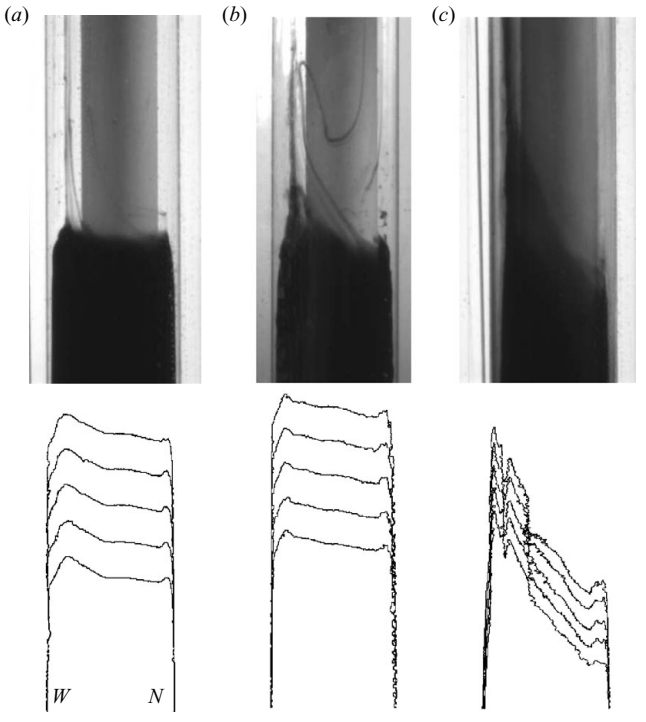

FIGURE 13. Displacement of two Newtonian fluids with $\kappa_1 = 1$, $\kappa_2 = 0.122$, $e = 0.25$ ($\delta = 0.084$): (*a*) $b = -0.222$; (*b*) $b = -0.111$; (*c*) $b = -0.056$. Below each image are the results of edge-detected interface at successive times along the annulus. The dimensionless distance between successive interfaces is (*a*) 0.26, (*b*) 0.25, (*c*) 0.14; (dimensional length scale is 47.4 mm). Physical parameters given in the text.

to the flow rate. What appears to be happening is that dispersion on the gap-scale promotes an axially advancing local finger towards the centre of the annular gap, at each azimuthal position, i.e. simply because the velocity is larger in the centre of the gap than at the walls. This finger must extend ahead of the mean position of the interface, and is thus influenced by the secondary azimuthal flows that exist. The displacing fluid is therefore swept azimuthally towards the wide side of the annulus, advancing the interface on that side. At larger flow rates the secondary flows are larger and the interface becomes increasingly elongated, although remaining steady. It is hard to make direct comparisons with the model results in terms of interface shape, due to optical distortion in processing the images. But we may approximately compare the axial extension of the interface along the annulus. In the model this is approximately 14 mm, at eccentricity of $e = 0.25$, which compares reasonably well with the extension at the largest value of $|b|$, but is much smaller than the axial extensions at smaller $|b|$. Clearly dispersion can have a significant effect.

4.3. *Combined effects: spikes and tails*

Although we have introduced dispersive effects above, by considering gap-scale and large-scale effects separately, in practice the effects occur simultaneously. This leads to a number of interesting flow observations. In the first place, the azimuthal secondary flow causes a focusing of fluid on the wide side, where it is swept ahead of the advancing front. As the flow across the gap is locally Poiseuille-like, the fluid that

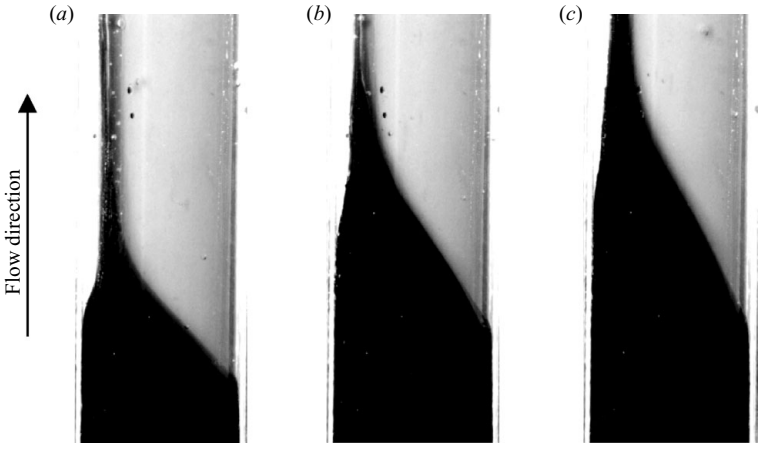

FIGURE 14. Spikes on the wide side in non-Newtonian displacements from series 4, at $e = 0.5$; (*a*) $\hat{Q} = 0.17$ L min^{-1}; (*b*) $\hat{Q} = 0.34$ L min^{-1}; (*c*) $\hat{Q} = 0.72$ L min^{-1}.

is focused on the wide side advances fastest in the centre of the gap in the form of a protruding spike. An example of this is shown in figure 14 (see also figure 13). These images are from series 4, at the highest eccentricity, $e = 0.5$, and show the phenomenon at increasing flow rates, for figure 14(*a–c*) respectively. At the two lower flow rates the displacement is steady but for the highest flow rate the displacement is unsteady, due to a diminished $|b|$. The spike on the wide side occurs for most displacements, regardless of rheology and whether steady or unsteady, with a varying degree of visibility. When the flow is unsteady it is hard to distinguish the advancing spike from the underlying unsteady interface. Even when steady the spike is observed to advance at many times the mean flow velocity.

More interesting and varied is the behaviour on the narrow side of the annulus. If we consider first a steady displacement, on the narrow side of the annulus we have a direct competition between gap-scale dispersion and the annular secondary flows. The former is advancing displacing (black) fluid ahead of the mean front position. The secondary flows on the other hand move backwards relative to the mean flow, hence stripping off displacing fluid from the sides of the advancing central finger and advecting this fluid towards the wide side. The net effect of this competition is a small spike, that sticks out ahead of the front (see figure 15). The spike is slightly longer and more visible at higher flow rates. It was observed in almost all Newtonian experiments, but not in non-Newtonian experiments (see e.g. figure 14). This may be because the gap-scale dispersion is reduced by both shear-thinning and yield stress effects, and hence the azimuthal currents dominate. We emphasize that this effect is wholly repeatable for steady displacements, on the narrow side.

The occurrence of spike-like interfaces has been observed before, e.g. by Petitjeans & Maxworthy (1996) and Scoffoni *et al.* (2001) in capillary tubes and by Lajeunesse *et al.* (1997, 1999) and Lajeunesse (1999) in plane channel/Hele-Shaw geometries. Petitjeans and Maxworthy relate the occurrence to a transition in the pattern of streamlines, as suggested by Taylor (1961). Lajeunesse and coworkers have developed a predictive methodology based on a lubrication displacement model. The regime in which they delineate spike formation is that in which buoyancy is dominant. Our case is different to both of these, in that the spikes appear to be governed by the secondary azimuthal flow, and the base tendency for the fluid to move faster in the

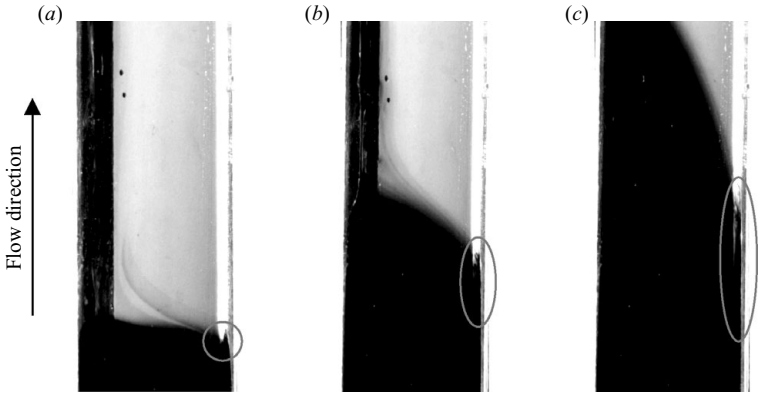

FIGURE 15. Spikes on the narrow side in Newtonian displacements from series 3, at $e = 0.5$; (*a*) $\hat{Q} = 0.17$ L min^{-1}; (*b*) $\hat{Q} = 0.34$ L min^{-1}; (*c*) $\hat{Q} = 0.72$ L min^{-1}.

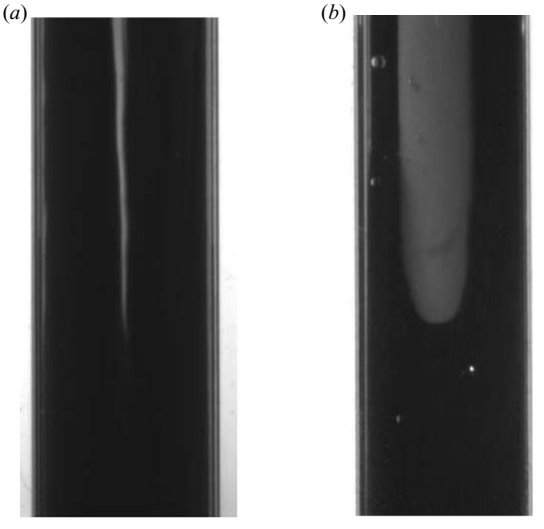

FIGURE 16. Examples of interface shape at rear of an unsteady displacement on the narrow side: (*a*) an example 'V' shape; (*b*) an example 'U' shape.

centre of the channel, rather than by buoyancy or by the recirculation dynamics on the gap scale.

In the case of unsteady displacements the narrow side behaviour is quite different as the mean interface position moves more slowly than the mean displacement speed. The interface elongates and the rear of the interface, at the narrow gap, typically showed either a 'V' or 'U' shape. The 'V' shape indicates that the interface is continually elongating in the narrow gap, whereas the 'U' shape indicates that the narrowest part is moving at a steady speed, over some range of azimuthal angles. These two features are illustrated in figure 16.

In the lubrication model developed by Pelipenko & Frigaard (2004*c*), there are parameter ranges for which the narrow side interface elongates progressively and others for which a shock forms and steady propagation is found. These two possibilities may correspond to the 'V' and 'U' shapes, but we have not carried out any systematic study. Tehrani *et al.* (1993) report observing a variety of behaviours

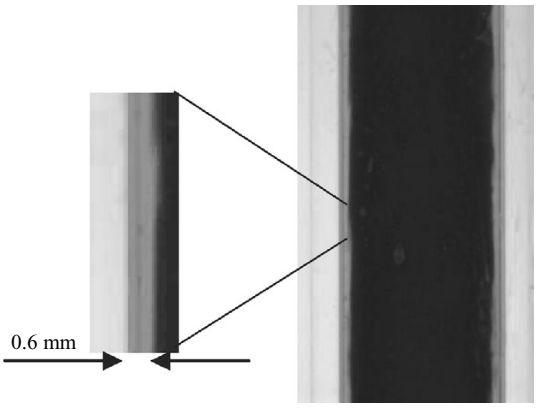

FIGURE 17. Drainage wall layer observed during a Newtonian displacement.

on the narrow side of the annulus, including a form of ribbing instability. As the interface elongates they identify a hydrostatic pressure imbalance as the driving force for azimuthal flows that may destabilize the narrow side. We have not observed this type of phenomenon in our experiments.

4.4. *Quantifying dispersion*

We have made some attempt to quantify dispersive effects, by comparing the spread of saturation times at lower and upper positions. However, apart from indicating that dispersion increases with both eccentricity and flow rate, these studies are largely inconclusive. This partly because we are far from the Taylor-dispersion regime, so that we don't have a simplistic model to 'fit', but also because we do not have enough experimental data to fit a new model.

4.5. *Other interesting phenomena*

In addition to the dispersion phenomena reported, several other effects were observed. Firstly, in many situations we have observed a thin drainage layer adjacent to the outer pipe wall, i.e. in the plane of the annular gap. Figure 17 shows a drainage layer of 0.6–1 mm in thickness. It is likely that a similar layer exists at the inner wall, but this is not visible. The drainage wall layer was most clearly visible for steady displacements when Xanthan displaced Carbopol. In experiments in our larger aspect ratio annulus, with lower viscosity pairs of Newtonian fluids, wall layers were observed to destabilize, with aperiodic wave undulations of wavelength 8–20 mm.

In displacements of yield stress fluids (series 5) at larger eccentricities it was common to find a channel of Carbopol left behind on the narrow side of the annulus. This phenomenon was first highlighted by McLean, Manry & Whitaker (1966) in the cementing context as a potential process problem. An example is shown in figure 18, taken form series 5. It is worth noting that in this flow, as the displacement is unsteady, azimuthal secondary flows are minimal and also the displaced fluid is static. Thus, dispersive currents are greatly reduced and we observe a very clean and sharp interface.

5. Discussion and conclusions

This paper has presented the results of 6 series of displacement flow experiments in narrow eccentric annuli. Each series consisted of displacements with the same fluid

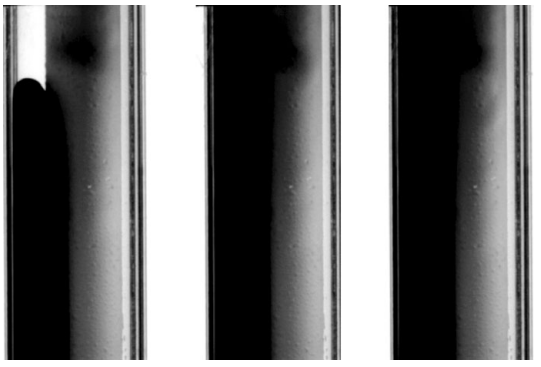

FIGURE 18. Static channel on the narrow side for an experiment in series 5: $e = 0.5$, $\hat{Q} = 0.34\,\mathrm{L\,min^{-1}}$. Images are shown at: 10, 45 and 75 s after opening of the gate valve.

pair, repeated at different eccentricities and different flow rates. The underlying results largely confirm the qualitative picture that underpins field-based 'rules of thumb' for the primary cementing of vertical wells (e.g. Couturier *et al.* 1990; Nelson & Guillot 2006). This same scenario has also been extensively studied in the context of a Hele-Shaw style displacement model by Bittleston *et al.* (2002) and Pelipenko & Frigaard (2004*a*,*b*,*c*). The overall trends observed are that (i) it is possible to have steady travelling wave displacement fronts in eccentric annular geometries, as well as unsteady displacements for which the interface elongates along the annulus; (ii) steadiness is promoted by a positive ratio of viscosity and density (i.e. displacing fluid more viscous and heavier), and by a smaller eccentricity.

The above falls into the realm of existing knowledge. More interesting and novel has been the observation of various secondary flow structures, that modify the displacement via dispersion. Two underlying processes combine to drive these flows. First, on the scale of the annular gap a Poiseuille-like velocity profile across the gap causes displacing fluid to advance in the centre faster than the mean position of the 'gap-averaged' interface. Secondly, secondary azimuthal flows produce a counter-current shear across the interface, in the case of a steady displacement. The size of the azimuthal secondary flow increases with the eccentricity. The secondary flow transports the advancing fingers of displacing fluid around to the wide side, where they frequently form a long finger/spike advancing locally ahead of the mean interface speed. The advance of this spike is due to the two dispersive tendencies acting together. A smaller spike may also sometimes form on the narrow side of the annulus, but does not grow in time. Here the azimuthal secondary flow opposes the gap-scale dispersive effects. Both effects are amplified by the flow rate.

We have characterized our experiments as either steady or unsteady by using the ratio of standard deviation to mean of the residence time distribution. We have also used other measurements from the local saturation curves to indicate how dispersive effects vary azimuthally. In the parameter regime where we operate we are far from a diffusive representation of dispersion (i.e. Taylor dispersion), but due to the geometric complexity of the flows it is hard to provide a simple characterization of advective effects. These measurements therefore give mostly qualitative information, principally confirming that dispersion manifests predominantly on the wide side of the annulus, in the presence of eccentricity.

In our Newtonian experiments, we note that increasing the flow rate has the effect of reducing $|b|$, which promotes unsteadiness, and also increases the amount of

azimuthal dispersion. Both destabilizing effects thus act together. We suspect therefore, that an unsteady displacement will elongate faster experimentally than predicted by the Hele-Shaw type of model (which has no gap-scale dispersion). On the other hand, the driving force for the azimuthal secondary currents is the mismatch between the far-field gap-averaged annular Poiseuille flow (which moves faster on the wide side), and a steadily propagating interface. Once the interface is not propagating steadily, we may expect that the azimuthal current decays as the interface elongates.

This leads naturally to the observation that in an eccentric annulus, even every steady interface is unsteady. The azimuthal secondary flow continues to pump displacing fluid towards the wide side, which then accelerates ahead of the front in the form of a spike. Whilst this can not be disputed we note that the spike is a local phenomenon and would not be present if there was no dispersion on the gap-scale. The absence of gap-scale dispersion leads to exactly the Hele-Shaw type of displacement flow. Therefore, we see that gap-scale dispersion is strongly modified by the azimuthal secondary flow. The reverse coupling is however not evident. Over wide ranges of flow parameters we have computed residence time distributions that have relatively constant $\sigma_{\Delta t}/\mu_{\Delta t} \ll 1$, over a broad range of parameters, only increasing sharply at some threshold value (see e.g. figure 9*d*). This suggests that the net result of the dispersion does not change the dynamics of the underlying large-scale Hele-Shaw flow. The failure of local 'interfacial' effects to modify the global flow is relatively commonplace in Hele-Shaw (and Darcy) flows (see e.g. Zimmerman & Homsy 1991). On the other hand there is some uncertainty about this conclusion since our experimental time scale is much shorter than that in the industrial application.

Whilst we suspect that the experimental displacement flows will be more unsteady than the computed Hele-Shaw displacements, with the same parameters, this is not straightforward to test. Experimentally there are numerous restrictions on the set of feasible experimental parameters. From the modelling perspective, it is time consuming and imprecise to determine a stability frontier from repetitive time-dependent simulations. Not least, this is because as the frontier is approached, growth rates approach zero, requiring very long times to infer stability or instability from simulation results. In Pelipenko & Frigaard (2004*c*) a semi-analytical approach is followed, in which a lubrication-style model is developed from the Hele-Shaw displacement model. This approach assumes an elongated interface has already developed and questions whether it would continue to grow. This gives semi-analytical bounds on sufficient conditions to be satisfied for the interface to grow indefinitely. In figure 19 we compare the predictions from this model with the experimental results. The regions that are predicted to be unsteady by the model in Pelipenko & Frigaard (2004*c*) are found to be unsteady for our experiments, but the prediction is clearly conservative with respect to the experiments, so caution must be exercised. Part of this conservatism stems from the lubrication model, i.e. this model predicts parameter regimes of unsteady displacements (which is where the model assumptions are self-consistent), but makes no prediction of the interface behaviour outside of these regimes.

In conclusion, the underlying dynamics of the Hele-Shaw style of model from Bittleston *et al.* (2002) do appear relevant to the experimental displacements. However, the experiments also expose a number of interesting dispersive effects that are simply not accounted for by the Hele-Shaw style of model. Our future plans in this domain include the attempt to include gap-scale dispersion within our present Hele-Shaw model, and then study its effects on the displacement. This will allow a more detailed comparison with the results presented here.

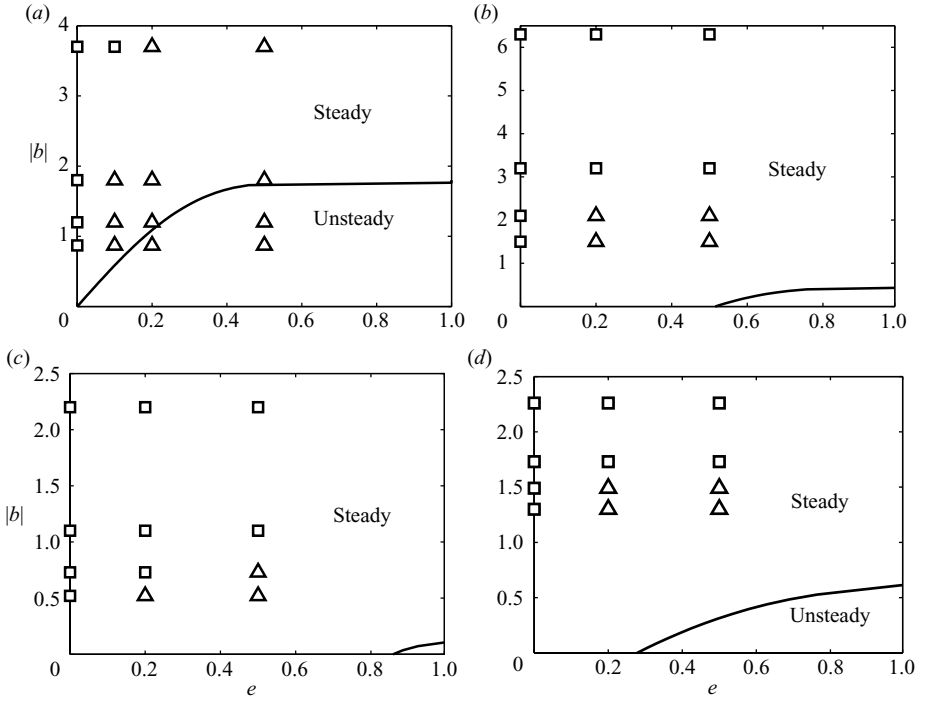

FIGURE 19. Comparison of the classified steady and unsteady experiments with the lubrication model predictions from Pelipenko & Frigaard (2004*c*): (*a*) series 1; (*b*) series 2; (*c*) series 3; (*d*) series 4.

This research has been carried out at the University of British Columbia, supported financially by NSERC and by Schlumberger. This support is gratefully acknowledged.

REFERENCES

ALLOUCHE, M., FRIGAARD, I. A. & SONA, G. 2000 Static wall layers in the displacement of two visco-plastic fluids in a plane channel. *J. Fluid Mech.* **424**, 243–277.

BITTLESTON, S. H., FERGUSON, J. & FRIGAARD, I. A. 2002 Mud removal and cement placement during primary cementing of an oil well; laminar non-Newtonian displacements in an eccentric Hele-Shaw cell. *J. Engng Math.* **43**, 229–253.

CHEN, C.-Y. & MEIBURG, E. 1996 Miscible displacements in capillary tubes. Part 2. Numerical simulations. *J. Fluid Mech.* **326**, 57–90.

COUTURIER, M., GUILLOT, D. J., HENDRIKS, H. & CALLET, F. 1990 Design rules and associated spacer properties for optimal mud removal in eccentric annuli. *Society of Petroleum Engineers*, paper number SPE 21594.

DUTRA, E., NACCACHE, M., SOUZA-MENDES, P., SOUTO, C., MARTINS, A. & DE MIRANDA, C. 2004 Analysis of interface between Newtonian and non-Newtonian fluids inside annular eccentric tubes. In *Proceedings of ASME-IMECE, November 2004*, Anaheim, CA. Paper number 59335.

ESCUDIER, M. P. & GOULDSON, I. W. 1995 Concentric annular flow with centrebody rotation of a Newtonian and a shear-thinning liquid. *Intl J. Heat Fluid Flow* **16**, 156–162.

ESCUDIER, M.P., GOULDSON, I.W. & JONES, D.M. 1995 Flow of shear-thinning fluids in a concentric annulus. *Exp. Fluids* **18**, 225–238.

ESCUDIER, M. P., GOULDSON, I. W., OLIVEIRA, P. J. & PINHO, F. T. 2000 Effects of inner cylinder rotation on laminar flow of a Newtonian fluid through an eccentric annulus. *Intl J. Heat Fluid Flow* **21**, 92–103.

Escudier, M. P., Oliveira, P. J. & Pinho, F. T. 2002*a* Fully developed laminar flow of non-Newtonian liquids through annuli: comparison of numerical calculations with experiments. *Intl J. Heat Fluid Flow* **23**, 52–73.

Escudier, M. P., Oliveira, P. J., Pinho, F. T. & Smith, S. 2002*b* Fully developed laminar flow of non-Newtonian liquids through annuli: comparison of numerical calculations with experiments. *Exp. Fluids* **33**, 101–111.

Frigaard, I. A., Scherzer, O. & Sona, G. 2001 Uniqueness and non-uniqueness in the steady displacement of two viscoplastic fluids. *ZAMM* **81** (2), 99–118.

Gabard, C. 2001 Etude de la stabilité de films liquides sur les parois d'une conduite verticale lors de l'ecoulement de fluides miscibles non-newtoniens. These de l'Universite Pierre et Marie Curie (PhD thesis), Orsay, France.

Gabard, C. & Hulin, J.-P. 2003 Miscible displacements of non-Newtonian fluids in a vertical tube. *Eur. Phys. J.* E **11**, 231–241.

Goyal, N. & Meiburg, E. 2006 Miscible displacements in Hele-Shaw cells: two-dimensional base states and their linear stability. *J. Fluid Mech.* **558**, 329–355.

Goyal, N. & Meiburg, E. 2007 Variable-density miscible displacements in a vertical Hele-Shaw cell: linear stability. *J. Fluid Mech.* **584**, 357–372.

Homsy, G. M. 1987 Viscous fingering in porous media. *Annu. Rev. Fluid Mech.* **19**, 271–311.

Jakobsen, J., Sterri, N., Saasen, A., Aas, B., Kjosnes, I. & Vigen, A. 1991 Displacements in eccentric annuli during primary cementing in deviated wells. *Society of Petroleum Engineers*, paper number SPE 21686.

Lajeunesse, E. 1999 Déplacement et instabilités de fluides miscibles et immiscibles en cellules de Hele-Shaw. These de l'Universite Pierre et Marie Curie (PhD thesis), Orsay, France.

Lajeunesse, E., Martin, J., Rakotomalala, N. & Salin, D. 1997 3D Instability of miscible displacements in a Hele-Shaw cell. *Phys. Rev. Lett.* **79**, 5254–5257.

Lajeunesse, E., Martin, J., Rakotomalala, N. & Salin, D. 2001 The threshold of the instability in miscible displacements in a Hele-Shaw cell at high rates. *Phys. Fluids* **13** (3), 799–801.

Lajeunesse, E., Martin, J., Rakotomalala, N., Salin, D. & Yortsos, Y. 1999 Miscible displacement in a Hele-Shaw cell at high rates. *J. Fluid Mech.* **398**, 299–319.

Long, P. J. G. 1991 Experimental studies of fluid-fluid displacement in annuli. PhD thesis, Cambridge University Press.

Martin, M., Latil, M. & Vetter, P. 1978 Mud displacement by slurry during primary cementing jobs – predicting optimum conditions. *Society of Petroleum Engineers*, paper number SPE 7590.

McLean, R. H., Manry, C. W. & Whitaker, W. W. 1966 Displacement mechanics in primary cementing. *Society of Petroleum Engineers*, paper number SPE 1488.

Naimi, M., Devienne, R. & Lebouché, M. 1990 Étude dynamique et thermique de lecoulement de Couette–Taylor–Poiseuille; cas dun fluide présentant un seuil découlement. *Intl J. Heat Mass Transfer* **33**, 381–391.

Nelson, E. B. & Guillot, D. 2006 *Well Cementing,* 2nd edn. Schlumberger Educational Services.

Nguyen, Q. D., Deawwanich, T., Tonmukayakul, N., Savery, M. R. & Chin, W. 2008 Flow visualization and numerical simulation of viscoplastic fluid displacements in eccentric annuli. In *AIP Conference Proceedings. XVth International Congress on Rheology: The Society of Rheology 80th Annual Meeting, July 7, 2008*, vol. 1027, pp. 279–281, Monterey, CA, doi:10.1063/1.2964662.

Nouar, M., Desaubry, C. & Zenaidi, H. 1998 Numerical and experimental investigation of thermal convection for a thermodependent Herschel–Bulkley fluid in an annular duct with rotating inner cylinder. *Eur. J. Mech.* B **17**, 875–900.

Nouar, M., Devienne, R. & Lebouché, M. 1987 Convection thermique pour lécoulement de Couette avec debit axial: cas dun fluide pseudoplastique. *Intl J. Heat Mass Transfer* **30**, 639–647.

Nouri, J. M., Umur, H. & Whitelaw, J. H. 1993 Flow of Newtonian and non-Newtonian fluids in concentric and eccentric annuli. *J. Fluid Mech.* **253**, 617–641.

Nouri, J. M. & Whitelaw, J. H. 1994 Flow of Newtonian and non-Newtonian fluids in a concentric annulus with rotation of the inner cylinder. *J. Fluids Engng* **116**, 821–827.

Nouri, J. M. & Whitelaw, J. H. 1997 Flow of Newtonian and non-Newtonian fluids in an eccentric annulus with rotation of the inner cylinder. *Intl J. Heat Fluid Flow* **18**, 236–246.

Pelipenko, S. & Frigaard, I. A. 2004*a* On steady state displacements in primary cementing of an oil well. *J. Engng Math.* **48** (1), 1–26.

Pelipenko, S. & Frigaard, I. A. 2004*b* Two-dimensional computational simulation of eccentric annular cementing displacements. *IMA J. Appl. Math.* **64** (6), 557–583.

Pelipenko, S. & Frigaard, I. A. 2004*c* Visco-plastic fluid displacements in near-vertical narrow eccentric annuli: prediction of travelling wave solutions and interfacial instability. *J. Fluid Mech.* **520**, 343–377.

Petitjeans, P. & Maxworthy, T. 1996 Miscible displacements in capillary tubes. Part 1. Experiments. *J. Fluid Mech.* **326**, 37–56.

Rakotomalala, N., Salin, D. & Watzky, P. 1997 Miscible displacement between two parallel plates: BGK lattice gas simulations. *J. Fluid Mech.* **338**, 277–297.

Schafroth, D., Goyal, N. & Meiburg, E. 2007 Miscible displacements in Hele-Shaw cells: nonmonotonic viscosity profiles. *Eur. Phys. J.* E **26**, 444–453.

Scoffoni, J., Lajeunesse, E. & Homsy, G. M. 2001 Interfacial instabilities during displacements of two miscible fluids in a vertical pipe. *Phys. Fluids* **13** (3), 553–556.

Taylor, G. I. 1961 Deposition of a viscous fluid on the wall of a tube. *J. Fluid Mech.* **10**, 161.

Tehrani, A., Bittleston, S. H. & Long, P. G. J. 1993 Flow instabilities during annular displacement of one non-Newtonian fluid by another. *Exp. Fluids* **14**, 246–256.

Tehrani, A., Ferguson, J. & Bittleston, S. H. 1992 Laminar displacement in annuli: a combined theoretical and experimental study. *Society of Petroleum Engineers*, paper number SPE 24569.

Vanaparthy, S. H. & Meiburg, E. 2008 Variable density and viscosity, miscible displacements in capillary tubes. *Eur. Phys. J.* E **27**, 268–289.

Vefring, E. H., Bjorkevoll, K. S., Hansen, S. A., Sterri, N., Saevareid, O., Aas, B. & Merlo, A. 1997 Optimization of displacement efficiency during primary cementing. *Society of Petroleum Engineers*, paper number SPE 39009.

Yang, Z. & Yortsos, Y. C. 1997 Asymptotic solutions of miscible displacements in geometries of large aspect ratio. *Phys. Fluids* **9** (2), 286–298.

Zhang, J. & Frigaard, I. A. 2006 Dispersion effects in the miscible displacement of two fluids in a duct of large aspect ratio. *J. Fluid Mech.* **549**, 225–251.

Zimmerman, W. B. & Homsy, G. M. 1991 Nonlinear viscous fingering in miscible displacements with anisotropic dispersion. *Phys. Fluids* **3**, 1859–1872.